Evaluation of Dual Domain Mass Transfer in Porous Media at the Pore Scale

by Leland Dorchester¹, Frederick D. Day-Lewis^{2,3}, and Kamini Singha⁴

Abstract

Dual-porosity models are often used to describe solute transport in heterogeneous media, but the parameters within these models (e.g., immobile porosity and mobile/immobile exchange rate coefficients) are difficult to identify experimentally or relate to measurable quantities. Here, we performed synthetic, pore-scale millifluidics simulations that coupled fluid flow, solute transport, and electrical resistivity (ER). A conductive-tracer test and the associated geoelectrical signatures were simulated for four flow rates in two distinct pore-scale model scenarios: one with intergranular porosity, and a second with an intragranular porosity also defined. With these models, we explore how the effective characteristic-length scale estimated from a best-fit dual-domain mass transfer (DDMT) model compares to geometric aspects of the flow field. In both model scenarios we find that: (1) mobile domains and immobile domains develop even in a system that is explicitly defined with one domain; (2) the ratio of immobile to mobile porosity is larger at faster flow rates as is the mass-transfer rate; and (3) a comparison of length scales associated with the mass-transfer rate (L_{α}) and those associated with calculation of the Peclet number (L_{Pe}) show L_{Pe} is commonly larger than L_{α} . These results suggest that estimated immobile porosities from a DDMT model are not only a function of physically mobile or immobile pore space, but also are a function of the average linear pore-water velocity and physical obstructions to flow, which can drive the development of immobile porosity even in single-porosity domains.

Introduction

To predict solute transport in porous media, the advection-dispersion equation (ADE) is commonly used. Because the ADE assumes Fickian spreading, it cannot predict "anomalous" behavior including late-time concentration tailing from the slow release of solutes and concentration rebound (e.g., Feehley et al. 2000; Levy and Berkowitz 2003; Major et al. 2011), which impede remediation efforts and drive up remediation costs at many contaminated sites in both fractured rock (e.g. Meigs and Beauheim 2001; Becker and Shapiro 2003; Liu et al. 2007; Kang et al. 2015, 2017; Nagare et al. 2020)

Article impact statement: Non-local transport model parameters are largely treated as fitting variables. Here, we explore their fundamental meaning at the pore scale.

Received December 2022, accepted May 2023. © 2023 National Ground Water Association. doi: 10.1111/gwat.13328

and porous media (e.g. Zheng et al. 2011; De Barros et al. 2013; Moradi and Mehdinejadiani 2018). Consequently, conceptual models that divide groundwater solute transport into multiple domains of differing connectivity to the main flowpath(s) have been shown to better describe transport in many systems (Harvey and Gorelick 2000; Karimi-Fard et al. 2006; Liu and Kitanidis 2012; De Dreuzy et al. 2013; Bolster et al. 2019).

One such conceptual model that breaks solute transport into two domains is dual-domain mass transfer (DDMT), which assumes the aguifer material can be described by two parameters beyond those in the ADE: an immobile porosity and the mass-transfer rate coefficient between the mobile and immobile porosity. In 2D, DDMT is described by:

$$\varepsilon_{m} \frac{\partial C_{m}}{\partial t} + \varepsilon_{im} \frac{\partial C_{im}}{\partial t} \\
= \varepsilon_{m} \left(\frac{\partial C_{m}}{\partial x} \left(D \frac{\partial C_{m}}{\partial x} \right) + \frac{\partial C_{m}}{\partial y} \left(D \frac{\partial C_{m}}{\partial y} \right) \right) \\
- \varepsilon_{m} \left(\frac{\partial u(x)C_{m}}{\partial x} + \frac{\partial u(y)C_{m}}{\partial y} \right), \tag{1a}$$

$$\varepsilon_{im} \frac{\partial C_{im}}{\partial t} = \alpha \left(c_{m} - c_{im} \right), \tag{1b}$$

where ε_m and ε_{im} are the mobile and immobile porosities [dimensionless], respectively; c_m and c_{im} are the

(1b)

¹Corresponding author: Hydrologic Science and Engineering Program, Colorado School of Mines, 1301 19th Street, Golden, CO 80401; Idorchester12@gmail.com

²Pacific Northwest National Laboratory, Earth Systems Science Division, 902 Battelle Boulevard, Richland, WA, 99352; frederick.day-lewis@pnnl.gov

³Department of Geophysics, Colorado School of Mines, Golden, CO; frederick.day-lewis@pnnl.gov

⁴Hydrologic Science and Engineering Program, Colorado School of Mines, 1301 19th Street, Golden, CO, 80401; ksingha@mines.edu

concentrations in the mobile and immobile porosities $[M/L^3]$, respectively; D is the hydrodynamic dispersion coefficient $[L^2/T]$, which is defined as the sum of mechanical dispersion (D_e) [L²/T] and molecular diffusion (D^*) $[L^2/T]$; u is the average linear pore water velocity in the x and v direction [L/T]; and α is the mass-transfer rate coefficient $[T^{-1}]$. In DDMT, the mobile domain porosity is defined as the fraction of aquifer where advection and dispersion occur, whereas the immobile domain porosity is the fraction where solute is stagnant and diffuses to/from the mobile domain. The ratio of the immobile to mobile porosity is referred to as β , the capacity coefficient. The mass-transfer rate coefficient, α , is a parameter that describes how easily mass can move between these porosities and is related to the characteristic diffusive length scale, L_{α} , by (Haggerty and Gorelick 1998):

$$L_{\alpha} = \sqrt{D^*/\alpha},\tag{2}$$

Other mass-transfer formulations consider diffusion to/from regions of various shapes, for example, spherical grains, as tabulated in Haggerty and Gorelick (1998). The mass-transfer rate is commonly determined by adjusting model variables until model results match the data (e.g., Rao et al. 1980; Knox et al. 2016). Despite notable previous work that employs DDMT models, one open question is what exactly "immobile" porosity means in many aquifer systems (e.g., Wheaton and Singha 2010; MahmoodPoor Dehkordy et al. 2018; Foster et al. 2021).

For this work, we consider two dimensionless numbers that are often used to determine the importance of advective, diffusive, and mass-transfer controls in groundwater systems. For example, the importance of the advective versus mass transfer is described by the Damkohler I number (Bahr and Rubin 1987):

$$DaI = \alpha \ (1+\beta) \frac{x}{u},\tag{3}$$

where x is the distance traveled from the solute source to the observation location [L]; thus, DaI is the ratio of advective time scale (x/u) to the time scale of mass transfer $([\alpha (1+\beta)]^{-1})$. Values of DaI > 1 and Da1 < 1 describe, respectively, zones where mass-transfer dominates and zones where advection dominates. One of the assumptions of the DDMT model is that immobile regions are diffusively controlled whereas mobile regions are advectively controlled. The relative roles of advection and diffusion are quantified by the dimensionless Peclet number:

$$Pe = \frac{L_{Pe}u_i}{D^*},\tag{4}$$

where L_{Pe} is the characteristic length [L] and u_i is the local velocity [L/T]. Thus, values of Pe > 1 and Pe < 1 describe zones of advectively and diffusively controlled transport, respectively (Bahr and Rubin 1987). Here, we look to explore how the ratio of diffusively to advectively controlled areas in the numerical models, based on the Peclet number, compare to estimated ratios of immobile

porosity to mobile porosity (β). While the Peclet number is commonly employed at the field scale, we follow previous work that has defined a local Peclet number at the pore scale (Hasan et al. 2019, 2020). What defines a characteristic length varies by investigation (Huysmans and Dassargues 2005), and it is an open question as to whether L_{Pe} is or should be related to L_{α} . Consequently, the goal of this work is to explore how immobile porosity is determined in systems when an immobile porosity is, and is not, explicitly defined.

One other complication is that although DDMT models have shown to fit experimental data better than the ADE in some cases (Feehley et al. 2000; Liu et al. 2010; Zheng et al. 2011; Liu and Kitanidis 2012), they include more unknown variables. Recent research has attempted to resolve the difficulty in parameterizing DDMT models by determining information on the immobile pore space by using fluid sampling coupled with electrical resistivity monitoring of conductive tracers (e.g., Singha et al. 2007). Fluid sampling from wells in the field preferentially draws from the mobile domain, therefore providing limited information on the immobile pore space whereas electrical resistivity is sensitive to the bulk composition of an aquifer. Therefore, electrical resistivity can be used in conjunction with co-located fluid sampling to infer the mass transfer rate and ratio of immobile/mobile porosity (e.g., Day-Lewis and Singha 2008). In particular, DDMT models can explain the hysteresis between the injection and flushing limbs on plots of fluid electrical conductivity versus bulk apparent electrical conductivity in the field (e.g., Singha et al. 2008; Briggs et al. 2013; Scruggs et al. 2019), in numerical studies (e.g., Wheaton and Singha 2010; Day-Lewis et al. 2017), and in laboratory work (e.g., Swanson et al. 2012, 2015; Foster et al. 2021). There have also been a number of excellent experimental papers recently looking at pore-scale studies of transport in millifluidics cells (De Anna et al. 2014; Jiménez-Martínez et al. 2015). Several of these papers used electrical monitoring (Jougnot et al. 2018; Visentini et al. 2023), including for reactive transport (Izumoto et al. 2022). Here, we also look to explore how the hysteresis between bulk apparent and fluid conductivity contribute to our qualitative, if not quantitative, understanding of mass transfer at this small scale.

We developed a pore-scale multiphysics numerical model in 2D to simulate (1) fluid flow, (2) solute transport, and (3) direct-current electrical conduction. Like others previous work (e.g., Jougnot et al. 2018; Visentini et al. 2023) a pore-scale model is formulated such that every pore and grain is represented explicitly so that we can systematically assess hydrologic parameters controlling solute transport and the response of electrical resistivity monitoring. However, we employ a pore-scale model so that we can explore how the mass transfer rate and immobile porosity are estimated in systems of varying complexity. Two saturated systems are simulated: one explicitly defined as a single domain with only intergranular porosity (i.e., the grains are impermeable and not porous), and another model defined

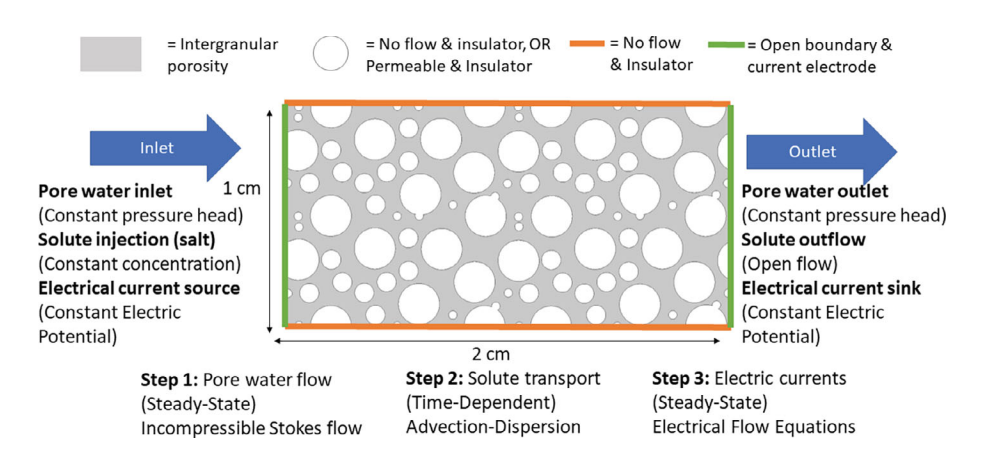


Figure 1. Physical representation of the water-saturated model domain. The gray space is defined as fluid and the white circles represent individual grains. The left border serves as the model inlet where groundwater, solute, and electrical current enter the domain, whereas the right border serves as the outlet for groundwater, solutes, and electrical current. The top and bottom boundaries, as well as grain surfaces, serve as no-flow boundaries and electrical insulators for the impermeable grains model scenario; however, in the second scenario, the grains are defined as permeable.

with an additional, intragranular porosity (i.e., the grains are permeable and porous); we refer to these as the impermeable-grains model scenario and permeable-grains model scenario hereafter. The impermeable grains model scenario replicates that of Liu and Kitanidis (2012), which enables comparison of our single-domain results to those previously published, although we add electrical conduction modeling to that scenario. We then extend that work by simulating permeable grains to explore systems with an explicitly defined secondary porosity. In both model scenarios, we add electrical conduction modeling and simulate a range of pressure gradients to observe how changes in the velocity impact the estimates of mass transfer and immobile porosity.

Model Setup and Equations

The 2D pore-scale model was created using COM-SOL Multiphysics 5.6, which uses the finite-element method to solve systems of partial differential equations (PDEs). As in Liu and Kitanidis (2012), the domain is defined as 1×2 cm with grains with radii of 0.090, 0.045, and 0.020 cm (Figure 1). Although the model domain was traced digitally, Liu and Kitanidis (2012) report a porosity of 0.41, whereas the model domain for this analysis was found to have a porosity of 0.51. The discrepancy in defined porosity may be because we traced a pixelated image of the model domain defined by Liu and Kitanidis (2012).

The model is assumed to be a plane view of a porous medium; therefore, the effects of gravity are neglected. For simulating fluid flow, solute transport, and the flow of electric currents, COMSOL Multiphysics solves the respective 3D PDEs by assuming the normal vector in the *z*-direction is 0, therefore simplifying to a 2D PDE. Resolving 3D PDEs in 2D allows the user to define more physically meaningful units like one might see in performing field or lab work; for example, concentration is defined as mol/m³ instead of mol/m².

Three physical processes are simulated: (1) steady-state fluid flow using Stokes flow (Equation 5a through 5c) when grains are impermeable and incorporating the Brinkman equations (Equation 6a through 6c) when grains are permeable, (2) transient solute transport via the ADE (Equations 7a, 7b, 8a, and 8b), and (3) steady-state electrical conduction assuming Ohm's law and current conservation (Equation 9a through 9c). We extract solute concentration (a proxy for fluid conductivity) and simulated electrical data from the model and use those data to calculate bulk conductivity and estimate mass transfer rates and immobile porosities. All parameters used in the numerical models are listed and described in Table A1 in Supplemental Material.

The pore-water velocity field throughout the model domain was determined using the COMSOL Creeping Flow Interface. It assumes incompressible Stokes flow, which neglects the inertial term in the Navier-Stokes equation under the assumption of non-turbulent flow for the impermeable grains model scenario. Therefore, when the model is defined as a single domain the pore-water velocity distribution can be described using

$$0 = \nabla \cdot (-pI + G) + F, \tag{5a}$$

$$\rho \nabla \cdot u = 0, \tag{5b}$$

$$G = \mu \left(\nabla u + (\nabla u)^T \right), \tag{5c}$$

where p is pressure (Pa), I is the identity matrix (–), G is the viscous stress tensor (Pa), F is the volume force vector (N/m³), ρ is the density of water (kg/m³), and μ is the dynamic viscosity of water (Pa·s).

The Brinkman equations (Equation 6a through 6c) are included when permeable grains are defined. Therefore, the Navier–Stokes equations are solved for the velocity and pressure field in open regions, and the Brinkman equations apply in the porous regions; at the interface between open regions and porous regions, velocity

and pressure are considered continuous (Le Bars and Worster 2006). The Brinkman equations combine the continuity equation and the momentum equation:

$$0 = \nabla \cdot [pI + G] - \left(\mu \kappa^{-1} + \frac{Q_m}{\varepsilon_p^2}\right) u + F, \qquad (6a)$$

$$\rho \nabla \cdot u = Q_m, \tag{6b}$$

$$G = \mu \frac{1}{\varepsilon_g} \left(\nabla u + (\nabla u)^T \right) - \frac{2}{3} \mu \frac{1}{\varepsilon_g} (\nabla \cdot u) I, \tag{6c}$$

where κ is the permeability tensor of the porous medium (m²), ε_g is the intragranular porosity (–), and Q_m is the mass source/sink (kg/[m³s]).

To solve for the movement of solutes throughout the domain, the velocity u is solved for as the dependent variable from the Navier-Stokes and Brinkman equations and incorporated as the independent variable of the ADE:

$$\frac{\partial c_i}{\partial t} + \nabla \cdot (M_i + uc_i) = R_i + S_i, \tag{7a}$$

$$M_i = -\left(D_e + D^*\right) \nabla c_{i,n},\tag{7b}$$

where c_i is the local concentration of species i (mol/m³), M_i is the mass flux relative to the mass averaged velocity (mol/[m²s]), R_i is the reaction rate for the species (mol/[m³s]), and S_i is an additional source/sink term (mol/[m³s]). R_i and S_i are defined as $0 \text{ mol/}(\text{m}^3\text{s})$ for our purposes. The mechanical dispersion coefficient D_e is also defined as $0 \text{ m}^2/\text{s}$ here. When an intragranular porosity is defined, Equations 7a and 7b are expanded to simulate pore-water concentrations in the intragranular porosity and intergranular porosity as:

$$\frac{\partial \left(\varepsilon_{g} c_{i,g}\right)}{\partial t} + \frac{\partial \left(\rho c_{i,p}\right)}{\partial t} + \nabla \cdot (M_{i} + u c_{i}) = R_{i} + S_{i}, \tag{8a}$$

$$M_{i} = -\left(D_{e} + \frac{\varepsilon_{g}}{\tau}D^{*}\right)\nabla c_{i,n},\tag{8b}$$

where $c_{i,g}$ is the local intragranular concentration, $c_{i,p}$ is the local intergranular concentration, and τ is the tortuosity (dimensionless) which is considered proportional to the cubic root of porosity, $\tau = \varepsilon_g^{-1/3}$.

Lastly, the electrical conduction is simulated as a current conservation problem where the solute concentration field is converted to fluid electrical conductivity using a linear transform where each 1 mg/L equates to 0.002 mS/cm (Keller and Frischknecht 1966). This equation was coupled with the molar mass of NaCl so that the conversion from concentration in mol/m³ to fluid electrical conductivity in S/m is represented by $58.44 \, \text{g/mol} \times 0.0002 \, \text{S/m}$. The Electric Currents interface solved for the electric potential at steady-state at a series of timesteps via the following equations:

$$\nabla \cdot J = Q_{j,v},\tag{9a}$$

$$J = \sigma E + J_e, \tag{9b}$$

$$E = -\nabla V, \tag{9c}$$

where J is the current density (A/m²) and the subscript e denotes an externally generated current density, $Q_{j,\nu}$ is the externally generated volumetric current source (A/m³), σ is the bulk electrical conductivity (S/m), E is the electric field, and V is the electric potential or voltage difference (V). It should be noted that $Q_{j,\nu}$ is invoked because the code assumes a unit (1 m) out-of-plane thickness for 2D simulations and the current is applied along the domain boundary which is therefore treated as a surface. A unit out-of-plane thickness for 2D simulations of electric currents is required to resolve the flow of electric currents, where the electric potential only varies in the x and y directions but is considered constant in the z direction (out-of-plane).

Model Boundary Conditions and Parameters

The physical parameters and boundary conditions of the impermeable-grains model scenario are shown in Figure 1 and Table 1 and are defined to reproduce those of Liu and Kitanidis (2012). In the model domain, the flow is defined as moving from left to right by a prescribed pressure gradient. The top and bottom boundaries are defined as no-flux boundaries. When grains are impermeable, they are defined with a no-slip condition.

For modeling solute transport and electric currents, several additional boundary conditions were defined (Figure 1). Solute is injected from the left boundary as a mass flux which defines the concentration at the inlet as 1.684 mol/m³ and the electric potential is defined as 0 V. At the right boundary, the solute is allowed to flow freely through an open boundary condition and the electric potential is defined as 1 V. Additionally, the top and bottom boundaries are defined as no-flux boundaries for both electric current and solute transport. Lastly, in the model scenario with impermeable grains, the grain boundaries are defined as electric insulators and no-flux boundaries. In the permeable-grains model scenarios, electric current and solutes can flow through the intragranular porosity of the grains; however, the grains themselves are electric insulators, so their electrical conductivity is a function of concentration.

Using a constant mass flux boundary condition, which behaves like a fixed concentration boundary condition at each timestep, we inject saline solute at 0.684 (background and flushing) and 1.684 (tracer injection) mol/m³. We define the initial background concentration before injection begins and during the flushing stage as 0.684 mol/m³, which corresponds to natural freshwaters (Fetter 2001), rather than 0 mol/m³ as in Liu and Kitanidis (2012). Defining the background concentration as greater than 0 mol/m³ prevents having a fluid with infinite electrical resistivity, which is unrealistic for the electrical simulations. Therefore, the domain concentration ranges between 0.684 mol/m³ and 1.684 mol/m³

Table 1
Physical Parameters and Boundary Conditions Used in the Coupled COMSOL Models

Parameter	Value	Parameter	Value
Inlet pressure head (p)	0.001, 0.01, 0.1, 1 Pa	Outlet pressure head (p)	0 Pa
Initial inlet/outlet concentration (c_0)	0.684mol/m^3	Injection concentration (c_i)	1.684mol/m^3
Inlet electric potential (V)	0 V	Outlet electric potential (V)	1 V
Fluid density (ρ)	1000kg/m^3	Dynamic viscosity of fluid (μ)	$8.9 \times 10^{-4} \text{ Pa-s}$
Diffusion coefficient (D_D)	$1 \times 10^{-9} \mathrm{m}^2/\mathrm{s}$	Dispersion coefficient (D_e)	$0 \mathrm{m}^2/\mathrm{s}$
Intragranular porosity (ε_g)	1%	Intragranular permeability (κ)	$1 \times 10^{-20} \text{m}^2$
Injection transition period	5 s		

All parameters are constant for every model scenario, except for the inlet pressure (p), intragranular porosity (ε_g) and intragranular permeability (κ) . The inlet pressure is adjusted to define the hydraulic gradient, whereas the intragranular porosity and permeability are defined to create the permeable grains model scenario.

Table 2
The Eight Model Scenarios Conducted

Model Scenario	Grain Parameters	Hydraulic Gradients
Models 1–4: Impermeable grains scenario	Grain permeability $(\kappa) = 0 \text{ m}^2$ Intragranular porosity $(\varepsilon_{\nu}) = 0\%$	5.1×10^{-6} , 5.1×10^{-5} , 0.00051, 0.0051
Models 5–8: Permeable grains scenario	Grain permeability $(\kappa) = 1 \times 10^{-20} \text{ m}^2$ Intragranular porosity $(\varepsilon_g) = 1\%$	5.1×10^{-6} , 5.1×10^{-5} , 0.00051, 0.0051

whereas the simulations of Liu and Kitanidis should range between 0 and 1 mol/m³. Saline injection was performed for 8.0 min in all models, which allowed near saturation of the model domain and was followed by a flushing period of equivalent duration with comparatively fresh water of $0.684 \, \text{mol/m}^3$ to remove solute from the model domain for the electrical simulations. Lastly, for both the impermeable- and permeable-grains scenarios, the pore-water flow regime is simulated at four pressure gradients (Table 2): 50, 5, 0.5, and 0.05 Pa/m, equivalent to hydraulic gradients of 5.1×10^{-6} , 5.1×10^{-5} , 0.00051, 0.0051, respectively (Table 2). This correlates to pore-water velocities ranging from $6.3 \times 10^{-7} \, \text{m/s}$ to $6.4 \times 10^{-4} \, \text{m/s}$, whereas Liu and Kitanidis (2012) considered velocities from $2.4 \times 10^{-8} \, \text{m/s}$ to $1.4 \times 10^{-6} \, \text{m/s}$.

Calculating the Bulk Apparent Conductivity of the Millifluidics Device

The bulk apparent conductivity of the domain is calculated from Ohm's law, where the electric potential is directly related to the product of electric current and resistance of the medium. To estimate the electrical resistance, the normal current density flux at the outlet is calculated, thus allowing for a time-dependent estimate of current at the outlet; additionally, the electric potential difference between the inlet and outlet is $1\,\mathrm{V}$ as defined in the boundary conditions. Lastly, as would be done in a field investigation, a homogeneous medium is assumed, and the geometric factor K [L] can be defined as follows

at the pore scale (Binley and Slater 2020):

$$K = A/w \tag{10}$$

where A is the cross-sectional area $[L^2]$, and w is the length [L] between the observed voltage difference. For this study, because the model is defined with a unit thickness, the geometric factor K is equal to $0.5 \, \text{cm}$. We note that the normal current density at the outlet is used instead of defining potential electrodes within the interior of the domain due to the scale of investigation. Additionally, we use the normal current density at the outlet because potential electrodes situated perpendicular to the direction of the potential gradient would induce a potential difference of $0 \, \text{V}$. The bulk apparent conductivity estimated via COMSOL is then plotted in time-series against the calculated fluid conductivity for mass transfer analyses of immobile porosity and mass-transfer rate (Singha et al. 2007; Briggs et al. 2014).

Improving the Numerical Stability of the Simulation

Several stabilization techniques were employed to minimize numerical instabilities in the model (e.g., Zheng and Bennett 2002). First, the concentration at the inlet was ramped up to the tracer concentration and back down to background concentration over 5 s using a numerically smoothed transition from 0.684 to 1.684 mol/m³. Injection of saline tracer, defined as 1.684 mol/m³, occurs between 20 s and 500 s, otherwise the background concentration of 0.684 mol/m³ is injected at all other times. Second, we include streamline and crosswind diffusion, which introduce numerical diffusion in the direction of, and orthogonal to, the transport direction (Zienkiewicz et al. 2013). Together, these efforts eliminated artificial oscillations in the breakthrough curves.

Fitting Analytic Solutions of the DDMT Equation

In all model simulations, an analytic solution of the 1D version of Equation 1 was fit to the advective flux of concentration from the outlet of the millifluidic cell. We use the multi-rate Laplace-domain code of Day-Lewis et al. (2017) to solve 1D transport within the column, representing all diffusion as mass transfer and assuming

a single rate and immobile domain. The Laplace-domain solution simplifies to:

$$\tilde{c}_{\rm m} = c_{\rm inj} \left[\frac{1}{s} - \frac{1}{s} exp \left(-T_{\rm off} s \right) \right]$$

$$\times exp \left[\frac{-xs}{v} \left(1 + \frac{\alpha \beta}{\alpha + s} \right) \right] H(x) + c_0, \quad (11a)$$

$$\tilde{c}_{\rm im} = \frac{\alpha \beta}{\alpha + s} c_{\rm im} + c_0, \tag{11b}$$

where $\tilde{c}_{\rm m}$ and $\tilde{c}_{\rm im}$ are the Laplace-transformed mobileand immobile-domain concentrations, respectively; H(x) is the Heaviside function; v is average linear pore fluid velocity; $T_{\rm off}$ is the time at which injection of tracer ends and flushing begins; and c_0 is the initial concentration, equal in both domains and uniform within each immobile compartment; and s is the Laplace parameter. The inverse Laplace transform is implemented using the de Hoog algorithm and code by Hollenbeck (1998).

To calculate the outlet concentration for use in parameterization of the 1D analytic model, we computed the advective flux as a line integral at the outlet, where the advective flux was considered analogous to transport predominantly contributed through mobileporosity pathways. The advective flux of concentration at the outlet is used for Equation 1, which is fit using a nonlinear least-square regression technique in MATLAB built on a trust-region-reflective algorithm (Coleman and Li 1996); this effectively equates the outlet concentration with what would be obtained via sampling from a representative elementary volume of dual-domain media. It iteratively adjusts the estimates of β and α until the magnitude of the residuals between the model output and the analytical solution is minimized. In addition to the fitting parameters β and α , the average linear velocity is required for the analytic solution; this is calculated based on the median arrival time of tracer at the outlet.

Peclet Analysis

We compare our β values estimated from the analytical solution to the ratio of area within the model

domain that is diffusively controlled versus advectively controlled as defined by a local Peclet number:

$$\beta_{pe} = \frac{\sum Pe_i < 1}{\sum Pe_i > 1}.\tag{12}$$

For the Peclet analysis, the velocity data were transferred from COMSOL to MATLAB on a regular grid that was spaced at 1140×570 points in the 2-cm by 1-cm domain. The Peclet analysis was performed as a binary assessment where Pe_i was calculated locally at each grid cell from Equation 4 using a parameter sweep over L_{Pe} . For each value of L_{Pe} , a local calculation of Pe_i was categorized as $Pe_i > 1$ or $Pe_i < 1$ and counted (Equation 12), thus allowing us to estimate areas of advectively or diffusively controlled transport. The parameter sweep was performed to determine the corresponding L_{Pe} at which β and β_{Pe} match. The range of L_{pe} was bounded between 1.07×10^{-3} cm and 2.00 cm, corresponding to twice the approximate side length of the smallest mesh element and the length of the millifluidics cell, respectively. As such, lengths that are slightly larger than the smallest spatial discretization, up to the distance between the source of the solute and observation (Huysmans and Dassargues 2005) are assessed. Lastly, we then compared the estimated L_{Pe} to L_{α} as calculated from Equation 2.

Results and Discussion

Considering two model scenarios of permeable grains and impermeable grains at four hydraulic gradients, the results of eight model iterations are discussed below.

Model Scenario with Impermeable Grains

Electrical Hysteresis

The characteristics of electrical conductivity hysteresis and thus the estimated DDMT parameters vary depending on the hydraulic gradient for the model scenario of impermeable grains. Given the four hydraulic gradients, the pore-water velocity at the outlet varies between 6.4×10^{-5} and 6.4×10^{-2} cm/s (Figure 2),

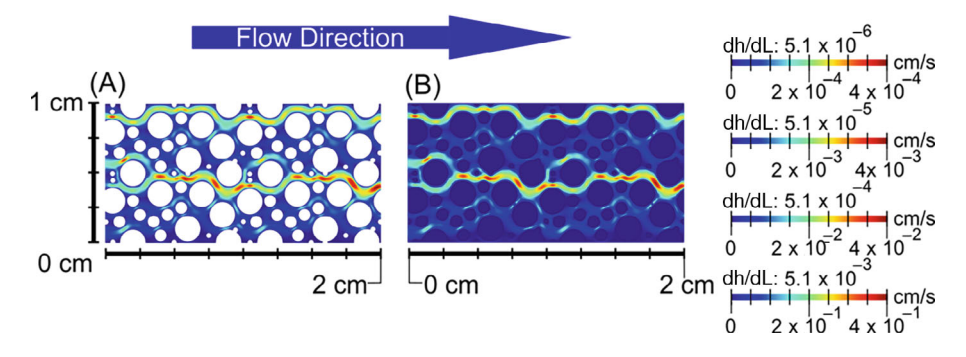


Figure 2. Pore-water flow regimes for the scenarios of: (A) impermeable grains, and (B) permeable grains. For both model scenarios, the pore-water velocity scales from 0 to 4×10^{-4} cm/s, 0 to 4×10^{-3} cm/s, 0 to 4×10^{-2} cm/s, and 0 to 4×10^{-1} cm/s for hydraulic gradients (dh/dL) of 5.1×10^{-6} , 5.1×10^{-5} , 5.1×10^{-4} , and 5.1×10^{-3} , respectively.

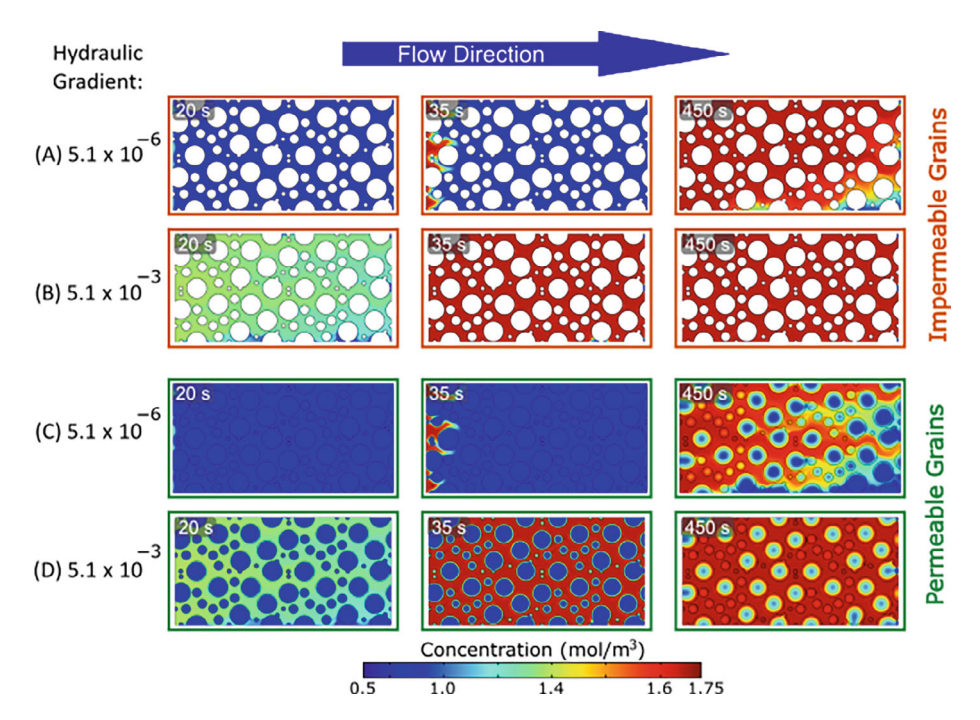


Figure 3. Concentration maps for the scenario of (A,B) impermeable grains, and (C,D) permeable grains. For both model scenarios, the two highest and lowest hydraulic gradients (dh/dL) are shown: 5.1×10^{-6} and 5.1×10^{-3} .

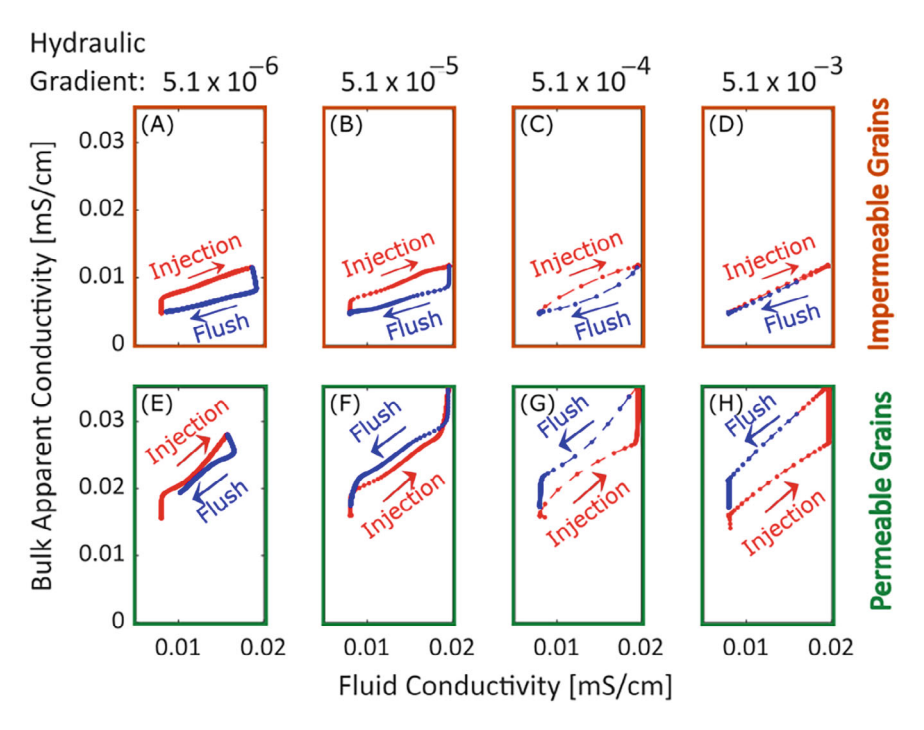


Figure 4. Hysteresis curves from plotting the bulk apparent versus fluid electrical conductivity in both model scenarios at various head gradients, where A-D are results from impermeable grains at head gradients of (A) 5.1×10^{-6} , (B) 5.1×10^{-5} , (C) 5.1×10^{-4} , (D) 5.1×10^{-3} and (E,F) are results from permeable grains at head gradients of (E) 5.1×10^{-6} , (F) 5.1×10^{-5} , (G) 5.1×10^{-4} , (H) 5.1×10^{-3} .

which drives expected changes in the concentration (Figures 3, S1 and S2). At the lowest hydraulic gradient of 5.1×10^{-6} , hysteresis between the fluid and bulk apparent conductivity occurs (Figure 4A), implying DDMT behavior even in the absence of a defined secondary porosity. As the hydraulic gradient is increased by

one and two orders of magnitude, the hysteresis behavior remains (Figure 4B and 4C), but as the hydraulic gradient is increased by three orders of magnitude, DDMT is reduced (Figure 4C) and eventually eliminated altogether at a hydraulic gradient of 0.0051 (Figure 4D), such that the fluid versus bulk apparent conductivity plots follow

a straight line. Hysteresis curves that collapse to a line (i.e., Archie's Law) suggest the absence of DDMT.

We additionally note that bulk apparent electrical conductivity changes faster than fluid electrical conductivity. thus creating a 'backwards' hysteresis loop. Backwards hysteresis occurs from difficulty in collocating the fluid and bulk apparent conductivity measurements because the model is defined at the pore scale, with the fluid sampling location defined at the outlet and the bulk apparent electrical conductivity measurements defined across the entire model domain from inlet to outlet. Several model iterations were performed with different configurations of current and potential electrodes, which sometimes produced backwards hysteresis between apparent bulk and fluid electrical conductivities. Backwards hysteresis, at this scale, results from a convolution of two issues: (1) difficulty with collecting collocated fluid and apparent bulk electrical conductivity measurements, and (2) a scale issue, where the scale associated with electrode measurements is not well suited to the scale of the model domain. Potential electrodes situated in diffusively or advectively dominated regions appeared to impact behavior of hysteresis. When the fluid sampling location is situated in an advective pathway, hysteresis proceeds in a "normal" direction, whereas when the fluid sampling location is situated in a more strongly diffusive pathway, hysteresis proceeds in a "backwards" direction. Briggs et al. (2014) discussed backwards hysteresis at the field scale extensively, attributing the behavior to non-collocated fluid and bulk apparent conductivity measurements. In a pore-scale numerical model, non-collocation is impossible to avoid. In our case, we see that observed change in the fluid electrical conductivity measurements is delayed by the time required for solute to travel across the model domain. In general, bulk apparent electrical conductivity measurements increase faster than the fluid electrical conductivity because the bulk apparent electrical conductivities are sensitive to the entire composition of the model domain.

Parameterizing the 1D Analytic Solution of the DDMT Equation

We estimated α and β by fitting the model concentration histories to the analytic solution of the DDMT equation, and then calculated the Dal for the bestfit parameters. The results of estimated α , β , and DaIexhibit several trends that imply more pronounced DDMT behavior at lower hydraulic gradients. As the hydraulic gradient increases from 5.1×10^{-6} to 0.0051, α increases from $0.018 \,\mathrm{s}^{-1}$ to $1.6 \,\mathrm{s}^{-1}$ (Figure 5A), β increases from 0.9 and 4.1 (Figure 5B), and DaI decreases from 4.6 to 2.0 (Figure 5C). These results are consistent with observations of hysteresis between the fluid and bulk apparent electrical conductivity, which show greater separation in the hysteresis curves at low flow (Figure 4A through 4D). β trends upwards with increasing flow, indicating the development of preferential flowpaths as pore-water velocity increases. At the fastest flow, DDMT is negligible. At low flows, we see: (1) slower mass transfer rate coefficients, (2) greater Damkohler numbers, and (3) greater separation between lines in the hysteresis curves.

Liu and Kitanidis (2012) similarly show that the effective mass-transfer rate coefficient increases non-linearly at higher velocity regimes; it can also be inferred from their work that estimated immobile porosity non-linearly increases with increasing velocity. Our results generally agree with theirs, which show increasing immobile porosity with velocity; however, we consider slightly higher velocities. On the other hand, at flows notably lower than assessed in this experiment, transport would likely be sufficiently characterized by the ADE because the model would become a diffusive transport problem (Liu and Kitanidis 2012). Although Liu and Kitanidis (2012) conclude that mobile porosity approaches an asymptotic value with increasing velocity our results do not reach an asymptote.

Model Scenario with Permeable Grains

Electrical Hysteresis

The results from modeling with permeable grains show more ideal hysteresis shapes, as described in previous work (Briggs et al. 2014). At the lowest hydraulic gradient of 5.1×10^{-6} (Figure 4E), the hysteresis pattern remains in a clockwise (i.e., "backward") direction, like all observable hysteresis results associated with the impermeable-grains model. However, as the hydraulic gradient increases to 5.10×10^{-5} (Figure 4F), the hysteresis pattern rotates weakly counterclockwise, indicating that the change in bulk apparent electrical conductivity is proceeding at a similar rate as change in fluid electrical conductivity. As the hydraulic gradient equals and exceeds 5.10×10^{-4} (Figure 4G and 4H), the fluid electrical conductivity changes at a faster rate than the bulk apparent electrical conductivity, with hysteresis in a more strongly counter-clockwise (i.e., "forward") direction. Faster change in fluid electrical conductivity than bulk apparent electrical conductivity indicates that solute is trapped in the permeable grains and leaches out, indicative of the presence of immobile porosity.

Parameterizing the 1D Analytic Solution of the DDMT Equation

We again observe clear trends in α and DaI and mixed results in β with different hydraulic gradients when parameterizing the analytic solution of the DDMT equation to the breakthrough curves produced from the permeable-grains model. As the hydraulic gradient increases from 5.1×10^{-6} to 5.1×10^{-3} , α increases from $1.7 \times 10^{-2} \, \mathrm{s^{-1}}$ to $1.8 \, \mathrm{s^{-1}}$ (Figure 5A), β increases from 1.0 and 4.1 (Figure 5B), and DaI decreases from 4.1 to 2.5 (Figure 5C). To establish a baseline estimate for β , we compare the analytical results for β (Figure 5B) to the ratio of intra- to intergranular porosity, which are assumed to be representative of the immobile and mobile porosities, respectively. The intragranular porosity is defined as 1% in COMSOL and the intergranular porosity is defined as 51%, thus leading to baseline estimated ratio

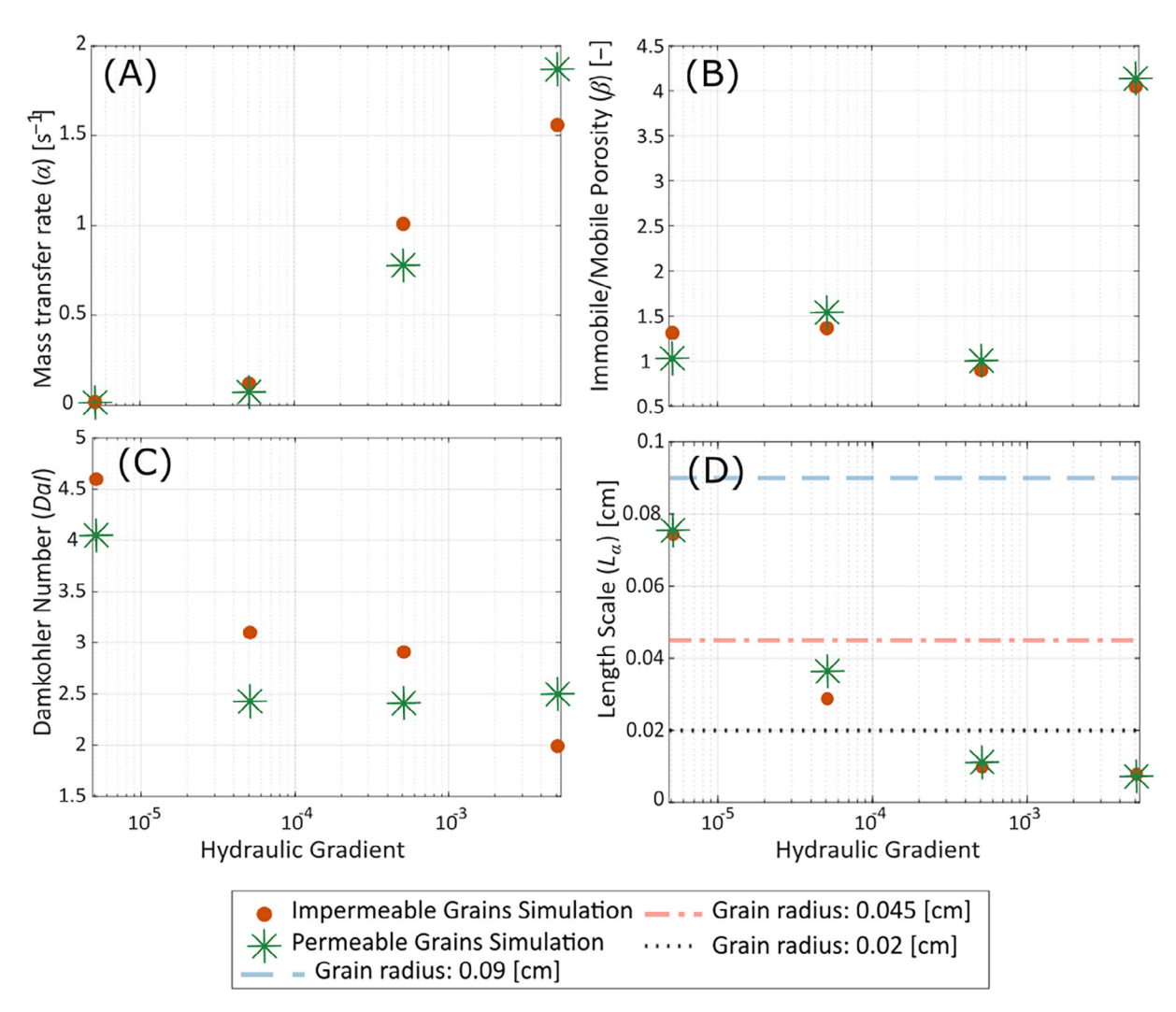


Figure 5. (A) mass transfer rates α , (B) ratios of immobile to mobile porosity β , (C) Damkohler number DaI, and (D) a characteristic length scale L_{α} and dominant grain radii for model scenarios of permeable and impermeable grains at four hydraulic gradients including 5.1×10^{-6} , 5.1×10^{-5} , 5.1×10^{-4} , 5.1×10^{-3} . Values for (A), (B), and (C) were produced from the linear least-squares regression parameterization of the 1D analytic solution of the DDMT equation (Equation 1) whereas values for (D) were produced by Equation 2. Grain radii are demarcated on (D) for comparison to estimated length scales.

of immobile/mobile porosity of 0.0097. The underestimate of this back-of-the-envelope calculation compared with the model-output results of 1.0-4.1 means that more zones of immobile porosity exist than can be estimated by the assigned porosities, likely because of some "dead end" pores on the leeward side of grains.

Comparison Between Permeable and Impermeable Grain Scenarios

We see clear differences when comparing the impermeable-grains scenario versus those of the permeable-grains scenario. First, when grains are permeable, we can see that the hysteresis curves between fluid and bulk apparent electrical conductivity are larger and show a more ideal shape at higher hydraulic gradients than the impermeable-grain hysteresis curves (Figure 4). Although we see electrical resistivity methods are sensitive to DDMT regardless of an explicitly defined secondary porosity at high hydraulic gradients, the

relationship of DDMT is obscured by a changing direction of hysteresis seen in the graphs when a secondary porosity is defined at lower hydraulic gradients. Therefore, we note that it can be difficult to reconcile the hysteretic relationship of non-local transport at the pore-scale due to issues of support volume as mentioned earlier.

Our results show that advective transport plays a larger role for the impermeable-grains scenario when compared to the permeable-grains scenario at the three lowest hydraulic gradients assessed. For three of four pore-water velocities, α is greater in the impermeable-grains scenario than for permeable-grains scenario (Figure 5A), likely because "immobile" zones are defined by slower-advection flowpaths, and because α is a function of average linear pore water velocity. This latter result was also seen in Liu and Kitanidis (2012) in their synthetic experiments, and the same hypothesis has been used to describe data in the field (e.g., Liu et al. 2007). The effective α is, consequently, controlled by what defines

the immobile porosity, whether larger-scale preferential pathways and/or intragranular porosity. Higher β exists when grains are permeable than when they are impermeable for three of four hydraulic gradients (Figure 5B); this is not surprising as one would expect higher immobile porosity to be present in a system where immobile porosity is explicitly defined. However, at the lowest hydraulic gradient in the impermeable-grains scenario, greater immobile pore space is estimated than in the permeable case, which could be attributed to a poorly parameterized analytic model as indicated by comparatively large root-mean-square error (RMSE) and percent bias (Table 3). Lastly, estimated DaI is always greater than 1 in these simulations, and larger in the impermeable-grains scenario than the permeable-grains scenario at the three lowest hydraulic gradients (Figure 5C). In contrast, at the highest hydraulic gradient of 0.0051, DaI is larger for the permeable-grains scenario than the impermeable-grains scenario, perhaps indicating that advection dominates in the impermeable-grains scenario at the highest hydraulic gradient whereas diffusion still contributes notably with the permeable grains. Lastly, we observe a decreasing trend in DaI as hydraulic gradients increase, which aligns with the understanding that the ratio of the diffusive to advective timescales is velocity dependent, with diffusion being increasingly important at lower velocity regimes.

Length-Scale Analysis

Coats and Smith (1964), among others, conceptualized the length scale from the definition of mass-transfer rate as the length over which diffusion occurs through a pore throat. However, our results show that the grain radii were a reasonable proxy regardless of grain permeability, which is in agreement with Haggerty et al. (2000). For the length-scale analysis, we explored the relations between L_{α} , calculated from the mass-transfer rate coefficient (Equation 2) and the grain radii. For the impermeableand permeable-grains model scenarios, the largest L_{α} were 0.075 and 0.076 cm and the smallest length scales were 0.0080 and 0.0073 cm, respectively (Figure 5D), which were in the general range of the smallest and largest grain radii, which were 0.020 and 0.090 cm, respectively. Furthermore, our results show a decreasing trend of L_{α} for both the permeable- and impermeable-grains model scenarios, indicating that L_{α} is a function of pore water velocity, in addition to geometric controls like grain size and grain permeability. Lastly, larger L_{α} observed at lower hydraulic gradients is attributed to increased importance of diffusion, compared to smaller L_{α} observed at higher hydraulic gradients, which correspond to more advectively dominated model conditions.

We also explored whether the ratio of diffusively to advectively controlled areas based on β_{Pe} (Equation 12, Figure 6) compared favorably to the estimated values of β from parameterizing Equation 1. β_{Pe} and β are similar in six out of eight simulations with only two results showing a percent difference of 10% or greater (Table 4). There are two values of β_{Pe} and β that are notably different, which are observed in the impermeable-grains

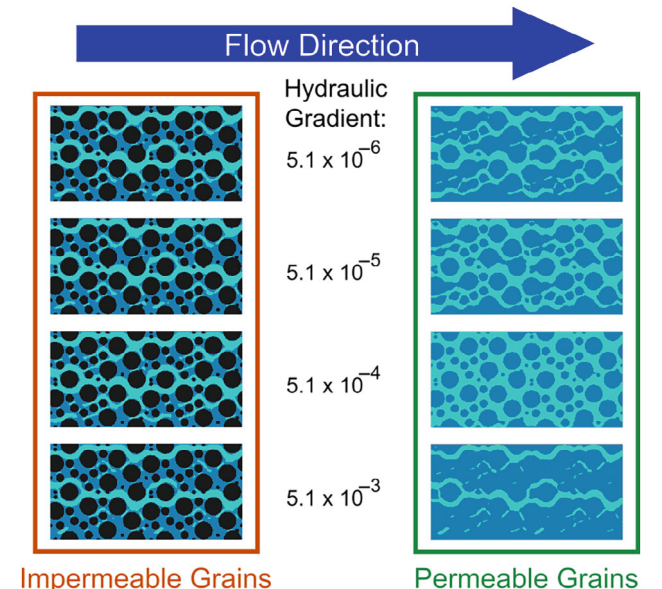


Figure 6. Results of calculating a local Peclet number (Equation 4), where areas of light blue are regions classified as advectively controlled transport, dark blue are regions of diffusively controlled transport, and black indicates impermeable grains. The ratio of the area of dark blue divided by the area of light blue represents estimated β_{Pe} (Equation 12).

model at the highest hydraulic gradient of 0.0051, and permeable-grains model at the lowest hydraulic gradient of 5.1×10^{-6} . For the model scenario of impermeable grains at a high hydraulic gradient, there are two explanations for poorly matching β_{Pe} and β , including (1) no hysteresis observed between fluid and bulk apparent EC measurements (Figure 4D), and (2) values of α , β , and DaI (Table 3) that indicate model conditions that are not well described by DDMT. The poor match in the model scenario of permeable grains at the lowest hydraulic gradient is likely because the calibrated 1D analytic DDMT model does not match the breakthrough curve well compared to other simulations (Table 3). This simulation exhibits "immobile" porosity in regions of intragranular porosity as well as between regions of preferential flow pathways (Figure 6E), and therefore may be better represented by a multi-rate mass transfer model rather than single-rate DDMT model. Besides these two cases, the remaining six scenarios had β_{Pe} that were comparable to β (Table 4, Figure 7B). In these six scenarios, the immobile porosity can be defined as diffusively controlled areas if an appropriate length scale (Equation 4) is determined. However, from these methods, immobile porosity can only be defined as diffusively controlled regions via numerically parameterizing Equation 12, therefore making these methods difficult to apply in a field setting. Nonetheless, our approach provides valuable, visual insight into the spatial pattern of the pore space where diffusively dominated transport occurs and constitutes immobile porosity.

We estimated L_{Pe} in all eight model simulations (Equation 4) which facilitated estimates of the ratio

dh/dL	Average Solute Velocity (m/s)	$\alpha \ (s^{-1})$	β (-)	<i>DaI</i> (-)	RMSE (-)	% Bias (-)
Impermeable gra	ains					
5.1×10^{-6}	0.00018	0.018	1.3	4.6	0.022	-0.89
5.1×10^{-5}	0.0018	0.12	1.4	3.1	0.009	0.015
0.00051	0.013	1.0	0.90	2.9	0.009	-0.0027
0.0051	0.04	1.6	4.1	2.0	0.011	-0.0054
Permeable grain	S					
5.1×10^{-6}	0.00018	0.017	1.0	4.1	11	-3.4
5.1×10^{-5}	0.0016	0.075	1.5	2.4	0.35	-0.068
0.0051	0.013	0.78	1.0	2.4	0.20	-0.0084
0.00051	0.02	1.9	4.1	2.5	0.80	-0.22

The associated goodness-of-fit metrics are calculated between the observed numerical breakthrough curve and the 1D analytic solution for the DDMT equation. Note the maximum values are bold, and minimum values are italicized for the root-mean-square error (RMSE) and % bias.

Table 4 Summary Results Comparing β_{pe} to β and L_{Pe} to L_{α}

Comparison of $\boldsymbol{\beta}$ and $\boldsymbol{\beta}_{pe}$					
Model Scenario	Hydraulic Gradient (–)	$oldsymbol{eta}$ from Parameterization of the Analytical DDMT Equation (–)	$ \beta_{pe} $ as Calculated from the Peclet Analysis $(-)$	% Difference Between β and β_{pe} (–)	Ratio of β_{pe}/β (-)
Impermeable grains	5.1×10^{-6}	1.3	1.3	0.023	1.0
	5.1×10^{-5}	1.4	1.4	0.42	1.0
	5.1×10^{-4}	0.90	0.93	3.6	1.0
	5.1×10^{-3}	4.1	1.8	78	0.44
Permeable grains	5.1×10^{-6}	1.0	2.4	<i>79</i>	2.3
, and the second	5.1×10^{-5}	1.5	1.5	0.0034	1.0
	5.1×10^{-4}	1.0	1.1	0.0023	1.0
	5.1×10^{-3}	4.1	4.5	9.1	1.1

Model Scenario	Hydraulic Gradient (–)	L_{Pe} (cm) Associated with Best Matching β_{pe} to β	L_{α} (cm) as Calculated form Equation 2	$\%$ Difference Between L_{Pe} and L_{α} (-)	Ratio of L_{Pe}/L_{α} (-)
Impermeable grains	5.1×10^{-6}	1.31	0.075	180	17
	5.1×10^{-5}	0.131	0.029	125	4.3
	5.1×10^{-4}	0.0161	0.0010	47	1.6
	5.1×10^{-3}	0.0011	0.0080	153	0.13
Permeable grains	5.1×10^{-6}	2.01	0.0761	185	26
-	5.1×10^{-5}	0.41	0.037	167	11
	5.1×10^{-4}	0.55	0.011	192	48
	5.1×10^{-3}	0.0011	0.0073	149	0.15

Values that may be potential outliers are bolded and italicized.

of diffusively to advectively controlled areas (β_{Pe} ; Equation 12). For the impermeable-grains scenario, the results show a good match between β_{Pe} and β for three out of four simulations. Our results show the minimum and maximum lengths of L_{Pe} that produce a match between β_{Pe} and β are estimated as 0.0011 and 1.3 cm, respectively. For the impermeable-grains scenario, L_{Pe} is estimated as 0.0011 cm at the highest hydraulic gradient of 5.1×10^{-3} , which is non-physical. This L_{Pe} , which falls on the bounds of the parameter sweep, is

not an adequate representation of the length scale for parameterizing Equation 12, as demonstrated by a percent difference between β_{Pe} and β of 78% (Table 4). However, at the other three hydraulic gradients, percent differences between β_{Pe} and β are less than 10% and were deemed acceptable matches.

The results for the permeable-grains scenario also show a good match between β_{Pe} and β for three out of four simulations. Our results show the minimum and maximum L_{Pe} estimated are 0.0011 and 2 cm, respectively,

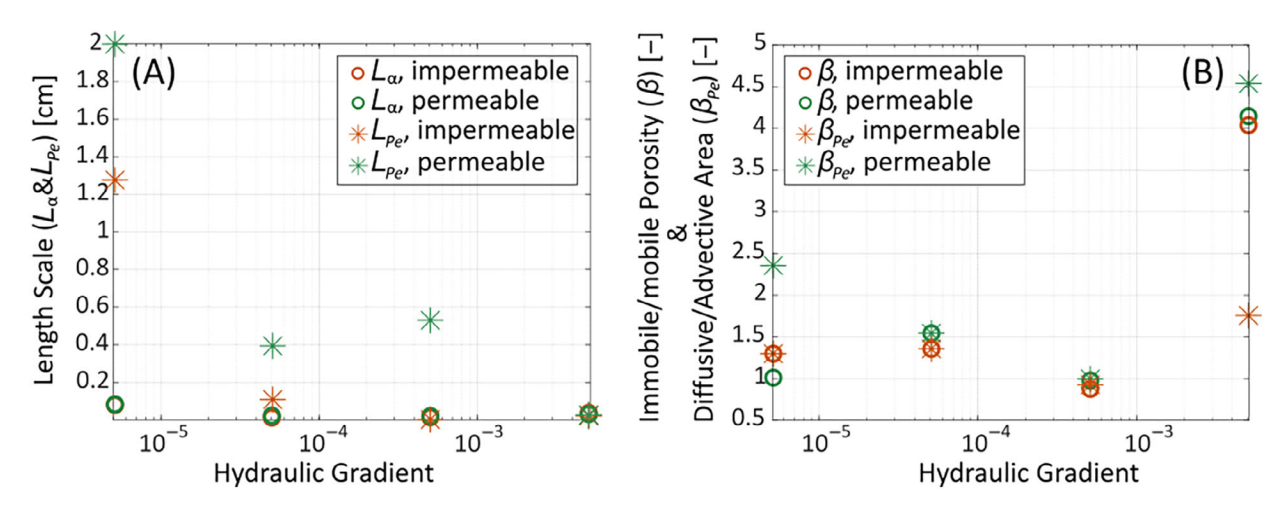


Figure 7. (A) Comparison of the diffusive length scale (L_{α} , Equation 2), with the Peclet length scale (L_{Pe}) (Equation 4), and (B) comparison of the ratio of immobile to mobile porosity estimated via analytically parameterizing the DDMT equation (Equation 1) to the estimated area of diffusively to advectively controlled areas (β_{Pe} , Equation 12) in the model domain.

which spans the bounds of the parameter sweep. However, only one problematic result is observed, which occurs at the lowest hydraulic gradient of 5.1×10^{-6} . At the lowest hydraulic gradient, an L_{Pe} of 2 cm is not an appropriate representation of the length scale as evidenced by the percent difference between β_{Pe} and β of 79%. The remaining three estimates of L_{Pe} for the impermeable-grains scenario are adequately described for Equation 12 as evidenced by percent differences between β_{Pe} and β that are less than 10%. Lastly, we note the estimate of L_{Pe} at the highest hydraulic gradient, is 0.0011 cm, which corresponds to the minimum bound of values considered in this analysis. We see that it is in the vicinity of the appropriate length scale, as demonstrated by the percent difference between β_{Pe} and β of 9%. Overall, for impermeable- and permeable-grains scenarios, we were able to estimate an reasonable L_{Pe} in six of eight simulations that describes the ratio of immobile to mobile porosity as the ratio of diffusively to advectively controlled areas.

Peclet Versus Diffusive Length Scales

We found a weak relationship between the magnitudes of the Peclet length scale L_{Pe} , the diffusive length scale L_{α} , and grain radii when β_{Pe} was parameterized to match β (Table 4). First, in both the impermeableand permeable-grain model scenarios, we see that L_{α} and L_{Pe} decrease as velocity increases. In each simulation we found that the difference between L_{Pe} and L_{α} was greatest at the lowest pore-water velocity. This difference decreases at intermediate velocities, whereas L_{α} is larger than L_{Pe} at the highest pore-water velocity (Table 4). The difference between L_{Pe} and L_{α} is more pronounced at lower hydraulic gradients for the impermeable-grains model scenario, whereas a similar relationship is less well defined for the permeable-grains model scenario. Collectively, these results show a weak relationship between L_{α} and L_{Pe} , where L_{Pe} is often one to two orders of magnitude larger than L_{α} and L_{α} is in the range of the dominant grain radii (Figure 5D).

The Peclet length scale L_{Pe} was required to estimate Equation 12 and used to compare ratios of diffusively to advectively controlled regions (β_{Pe}) with ratios of immobile to mobile porosity (β) . From our analysis, we find that the immobile porosity can be defined as diffusively controlled areas in six of eight model scenarios; however, this is a numerical result that is dependent on L_{Pe} , not one based on geometric characteristics of the pore space. Therefore, investigating the relationship between L_{Pe} and associated hydrologic parameters, like the characteristic diffusive length scale L_{α} and/or pore-water velocity, may prove useful in parameterizing DDMT models from physical measurements obtained from the field or laboratory. Furthermore, defining the relationship between L_{Pe} and associated hydrologic parameters, could help extend these methods to the field system. We estimated L_{Pe} by exploring a wide range of lengths due to the wide range of definitions for a Peclet number. The variety of definitions of Peclet numbers and subsequent length scales is thoroughly discussed by Huysmans and Dassargues (2005), who note that L_{Pe} is problem dependent but can be defined variously including as (1) the distance from source of contamination to observation, (2) the waste container radius, (3) the pore/fracture size, or (4) the average particle diameter, among others. Therefore, because the length scale used in calculating a Peclet number is not straightforward, it seems prudent to continue working to define what an appropriate length scale is when defining a Peclet number in the context of DDMT. Defining L_{Pe} may help practicing engineers and scientists establish a framework that helps better define advective versus diffusive controls in a groundwater system and may even help define ratios of immobile to mobile porosity.

Conclusions

Dual-porosity models are often used to describe solute transport in field systems, but the parameters within

these models are difficult to identify experimentally or relate to measurable quantities. Here, we sought to explore how (1) a DDMT model fits simulated data in the presence and absence of explicit immobile porosity and (2) the effective characteristic length scale based on both diffusive mass transfer (L_{α}) and the Peclet number (L_{Pe}) compares to geometric aspects of pore structure and the velocity field. We have three primary conclusions: (1) mobile and immobile domains develop even in a system that is explicitly defined with one domain; (2) the ratio of immobile to mobile porosity and mass-transfer rate coefficients are smaller at slower flow rates; and (3) a comparison of length scales associated with the masstransfer rate (L_{α}) and those associated with calculation of the Peclet number (L_{Pe}) show L_{Pe} is typically larger than L_{α} by one to two orders of magnitude.

With respect to our first conclusion, our results show the presence of immobile porosity regardless of whether it is explicitly defined. This conclusion is drawn from the hysteresis between fluid and bulk apparent electrical conductivity observed in seven of eight models and was confirmed by parameterizing a 1D analytic solution of the DDMT equation to concentration breakthrough curves. The presence of DDMT is dictated, at minimum, by two physical properties: (1) physical geometric controls like dead-end pores, and (2) presence of differently advective transport pathways.

In terms of the second conclusion, we find that estimates of β , α , and DaI are functions of average linear pore-water velocity. We note that the distribution of the velocity field does not change with gradient; however, where Pe is greater or less than 1 will change. β , α , and DaI qualitatively relate to the hysteresis curves produced, which have more separated limbs at lower velocities than higher velocities. In the presence of explicit intragranular porosity, α and β increase non-linearly as the average linear pore-water velocities increase, whereas DaI decreases. This finding is consistent with previous investigations and underscores the importance of considering time-varying hydraulic conditions when parameterizing DDMT models.

Lastly, we attempted to define immobile porosity in terms of the area of the millifluidics cell where diffusion was dominant, by comparing our estimates of β from the 1D analytical solution to the DDMT model to β_{Pe} estimated throughout the domain. While six out of eight model scenarios show that the immobile porosity can be defined by diffusively dominated regions via similar β and β_{Pe} , it is difficult to proactively apply this idea in the field because we see that L_{Pe} is velocity dependent and it deviates from previous definitions of the length scale used to estimate a Peclet number.

These results suggest that estimated immobile porosities from a DDMT model are not only a function of diffusion-accessible pore space, but also are a function of average linear pore-water velocity and geometric controls, such as obstructions to flow that cause less-advective pathways. This work demonstrates that the definition of "immobile" is a function of the pore-water velocity and domain geometry, where physical obstructions to flow can control the presence of advective and diffusive pathways, and demonstrates that the complicated dependence of transport on hydraulic gradient and the exact configuration of preferential flowpaths makes it difficult to extrapolate dual-porosity models calibrated in one situation to unexplored configurations such as might be imposed for remediation or solute extraction. While DDMT is a useful model for predicting solute transport, the definition of immobile pore space remains difficult to interpret, even at the pore scale, and subsequently in field investigations as well.

Acknowledgments

F.D.D.L. was supported by the Energy and Environment Mission Seed Program, under the Laboratory Directed Research and Development (LDRD) Program at Pacific Northwest National Laboratory (PNNL). PNNL is a multi-program national laboratory operated for the U.S. Department of Energy (DOE) by Battelle Memorial Institute under Contract No. DE-AC05-76RL01830. This work was also supported in part by National Science Foundation grant EAR-2012730.

Authors' Note

The authors do not have any conflicts of interest or financial disclosures to report.

Disclaimer

Supporting Information is generally *not* peer reviewed.

APPENDIX

The following table displays all parameters that were used in this work. It is grouped by parameters used to simulate three physical processes of fluid flow, solute transport, and electric currents. There is one additional section for the analytic modeling of solute transport via the DDMT equation.

Table A1 Model Parameters

Variables	Parameter	Variables	Parameter
For the mod	leling of fluid flow using the Navier-Stokes and Bri	nkman's equa	ations
ρ	Fluid density (kg/m ³)	и	Velocity vector (m/s)
p	Pressure (Pa)	μ	Dynamic viscosity of fluid $(kg/[m \times s])$
I	Identity matrix	ε_g	Intragranular porosity
F	Volume force vector (N/m ³)	κ	Permeability tensor of the porous medium
G	Viscous stress tensor (Pa)	Q_m	Mass source or sink (kg/(m ³ s))
For the mod	eling of solute transport using mass conservation ed	uations	
c_i	Local node concentration of species $i \pmod{m^3}$	S_i	Source/sink term (mol/(m ³ s))
c_0	Initial inlet concentration (mol/m ³)	$c_{i,g}$	Local intragranular concentration of species $i \pmod{m^3}$
$c_{i,p}$	Local intergranular concentration of species <i>i</i> (mol/m ³)	$D_{D,i}$	Effective diffusion coefficient (m ² /s)
M_i	Mass flux relative to the mass averaged velocity (mol/[m ² s])	$D_{e,i}$	Effective dispersion coefficient (m ² /s)
R_i	Reaction rate of species $i \pmod{(m^3s)}$		
For the mod	eling of electric currents		
J	Current density (A/m ²) where the additional subscript 'e' denotes externally generated	σ	Electrical conductivity (S/m)
$Q_{i,v}$	Externally generated current source (A/m ³)	V	Electric potential (Voltage, V)
\tilde{E}	Electric field	K	Geometric factor
For the anal	ytic modeling of dual-domain mass-transfer behavio	r	
$\varepsilon_{m,im}$	Mobile and immobile porosity (–)	arepsilon	Total porosity (–)
$C_{m,im}$	Mobile and immobile concentration (mol/m ³)	α	Mass transfer rate (s ⁻¹)
D	Hydrodynamic dispersion coefficient (m ² /s)	β	Ratio of immobile to mobile porosity (–)
D^*	Molecular diffusion constant (m ² /s)	eta_{Pe}	Ratio of diffusively controlled zones to advectively controlled zones
Pe	Local Peclet number at the i^{th} location	L_{Pe}	Advective length scale (cm) associated with solute transport
u_i	Local velocity magnitude	L_{lpha}	Diffusive length scale (m) associated with mass transfer
DaI	Damkohler number (-)		

Supporting Information

Additional supporting information may be found online in the Supporting Information section at the end of the article. Supporting Information is generally *not* peer reviewed.

Data S1. Supporting Information.

Figure S1. Concentration distribution for seven timesteps at each hydraulic gradient for the impermeable grains model scenario. Saline injection begins at 20 s, it spans 8 min, and has a five second transition period between the injection and flushing period. Note, the figures do not show the flushing period.

Figure S2. Concentration distribution for seven timesteps at each hydraulic gradient for the permeable grains model scenario. Saline injection begins at 20 s, it spans 8 min, and has a five second transition period between the injection and flushing period. Note, the figures do not show the flushing period.

References

Bahr, J.M., and J. Rubin. 1987. Direct comparison of kinetic and local equilibrium formulations for solute transport affected by surface reactions. *Water Resources Research* 23, no. 3: 149–173. https://doi.org/10.1029/WR023i003p00438

Becker, M.W., and A.M. Shapiro. 2003. Interpreting tracer breakthrough tailing from different forced-gradient tracer experiment configurations in fractured bedrock. *Water Resources Research* 39, no. 1: 1–13. https://doi.org/10.1029/2001WR001190

Binley, A., and L.D. Slater. 2020. Resistivity and Induced Polarization: Theory and Applications to the Near-Surface Earth. Cambridge, UK: Cambridge University Press.

Bolster, D., K.R. Roche, and V.L. Morales. 2019. Recent advances in anomalous transport models for predicting contaminants in natural groundwater systems. *Current Opinion in Chemical Engineering* 26: 72–80. https://doi.org/10.1016/j.coche.2019.09.006

Briggs, M.A., F.D. Day-Lewis, J.B. Ong, J.W. Harvey, and J.W. Lane. 2014. Dual-domain mass-transfer parameters from electrical hysteresis: Theory and analytical approach applied to laboratory, synthetic streambed, and ground-

- water experiments. Water Resources Research 50, no. 10: 8281–8299. https://doi.org/10.1002/2014WR015880
- Briggs, M.A., F.D. Day-Lewis, J.B.T. Ong, G.P. Curtis, and J.W. Lane. 2013. Simultaneous estimation of local-scale and flow path-scale dual-domain mass transfer parameters using geoelectrical monitoring. *Water Resources Research* 49, no. 9: 5615–5630. https://doi.org/10.1002/wrcr.20397
- Coats, K.H., and B.D. Smith. 1964. Dead-end pore volume and dispersion in porous media. *Society of Petroleum Engineers Journal* 4, no. 1: 73–84. https://doi.org/10.2118/647-pa
- Coleman, T.F., and Y. Li. 1996. An interior trust region approach for nonlinear minimization subject to bounds. *SIAM Journal on Optimization* 6, no. 2: 418–445. https://doi.org/10.1137/0806023
- Day-Lewis, F.D., N. Linde, R. Haggerty, K. Singha, and M.A. Briggs. 2017. Pore network modeling of the electrical signature of solute transport in dual-domain media. *Geophysical Research Letters* 44, no. 10: 4908–4916. https://doi.org/10.1002/2017GL073326
- Day-Lewis, F.D., and K. Singha. 2008. Geoelectrical inference of mass transfer parameters using temporal moments. *Water Resources Research* 44, no. 5: 1–6. https://doi.org/10.1029/2007WR006750
- De Anna, P., J. Jimenez-Martinez, H. Tabuteau, R. Turuban, T. Le Borgne, M. Derrien, and Y. Méheust. 2014. Mixing and reaction kinetics in porous media: An experimental pore scale quantification. *Environmental Science & Technology* 48, no. 1: 508–516.
- De Barros, F.P.J., D. Fernàndez-Garcia, D. Bolster, and X. Sanchez-Vila. 2013. A risk-based probabilistic framework to estimate the endpoint of remediation: Concentration rebound by rate-limited mass transfer. Water Resources Research 49, no. 4: 1929–1942. https://doi.org/10.1002 /wrcr.20171
- De Dreuzy, J.R., A. Rapaport, T. Babey, and J. Harmand. 2013. Influence of porosity structures on mixing-induced reactivity at chemical equilibrium in mobile/immobile Multi-Rate Mass Transfer (MRMT) and Multiple INteracting Continua (MINC) models. *Water Resources Research* 49, no. 12: 8511–8530. https://doi.org/10.1002/2013WR013808
- Feehley, C.E., C. Zheng, and F.J. Molz. 2000. A dual-domain mass transfer approach for modeling solute transport in heterogeneous aquifers: Application to the macrodispersion experiment (MADE) site. *Water Resources Research* 36, no. 9: 2501–2515. https://doi.org/10.1029/2000WR900148
- Fetter, C.W. 2001. Applied Hydrogeology, 4th ed. NJ: Upper Saddle River, Prentice-Hall, Inc.
- Foster, A., A.C. Trautz, D. Bolster, T. Illangasekare, and K. Singha. 2021. Effects of large-scale heterogeneity and temporally varying hydrologic processes on estimating immobile pore space: A mesoscale-laboratory experimental and numerical modeling investigation. *Journal of Contaminant Hydrology* 241, no. 2021: 103811. https://doi.org/10.1016/j.jconhyd.2021.103811
- Haggerty, R., S.A. McKenna, and L.C. Meigs. 2000. On the late-time behavior of tracer test breakthrough curves. Water Resources Research 36, no. 12: 3467–3479. https://doi.org/10.1029/2000WR900214
- Haggerty, R., and S.M. Gorelick. 1998. Modeling mass transfer processes in soil columns with pore-scale heterogeneity. *Soil Science Society of America Journal* 62, no. 1: 62–74. https://doi.org/10.2136/sssaj1998.03615995006200010009x
- Harvey, C., and S.M. Gorelick. 2000. Rate-limited mass transfer or macrodispersion: Which dominates plume evolution at the macrodispersion experiment (MADE) site? Water Resources Research 36, no. 3: 637–650. https://doi.org/10 .1029/1999WR900247
- Hasan, S., V. Niasar, N.K. Karadimitriou, J.R.A. Godinho, N.T. Vo, S. An, A. Rabbani, and H. Steeb. 2020. Direct

- characterization of solute transport in unsaturated porous media using fast X-ray synchrotron microtomography. *Proceedings of the National Academy of Sciences of the United States of America* 117, no. 38: 23443–23449. https://doi.org/10.1073/pnas.2011716117
- Hasan, S., V. Niasar, N.K. Karadimitriou, and M. Sahimi. 2019. Saturation dependence of non-Fickian transport in porous media. Water Resources Research 55, no. 2: 1153–1166. https://doi.org/10.1029/2018WR023554
- Hollenbeck, K. J. 1998. INVLAP.M: A Matlab Function for Numerical Inversion of Laplace Transforms by the de Hoog Algorithm. Accessed February 3, 2022. http://www.isva.dtu .dk/staff/karl/invlap.htm
- Huysmans, M., and A. Dassargues. 2005. Review of the use of Péclet numbers to determine the relative importance of advection and diffusion in low permeability environments. *Hydrogeology Journal* 13, no. 5–6: 895–904. https://doi.org/10.1007/s10040-004-0387-4
- Izumoto, S., J.A. Huisman, E. Zimmermann, J. Heyman, F. Gomez, H. Tabuteau, R. Laniel, H. Vereecken, Y. Meheust, and T. Le Borgne. 2022. Pore-scale mechanisms for spectral induced polarization of calcite precipitation inferred from geo-electrical millifluidics. *Environmental Science & Technology* 56, no. 8: 4998–5008.
- Jiménez-Martínez, J., P. de Anna, H. Tabuteau, R. Turuban, T.L. Borgne, and Y. Méheust. 2015. Pore-scale mechanisms for the enhancement of mixing in unsaturated porous media and implications for chemical reactions. *Geophysical Research Letters* 42, no. 13: 5316–5324.
- Jougnot, D., J. Jiménez-Martínez, R. Legendre, T. Le Borgne, Y. Méheust, and N. Linde. 2018. Impact of small-scale saline tracer heterogeneity on electrical resistivity monitoring in fully and partially saturated porous media: Insights from geoelectrical milli-fluidic experiments. Advances in Water Resources 113: 295–309. https://doi.org/10.1016/j .advwatres.2018.01.014
- Kang, P.K., M. Dentz, T. Le Borgne, S. Lee, and R. Juanes. 2017. Anomalous transport in disordered fracture networks: Spatial Markov model for dispersion with variable injection modes. Advances in Water Resources 106: 80–94. https://doi.org/10.1016/j.advwatres.2017.03.024
- Kang, P.K., M. Dentz, T. Le Borgne, and R. Juanes. 2015. Anomalous transport on regular fracture networks: Impact of conductivity heterogeneity and mixing at fracture intersections. *Physical Review E - Statistical, Nonlinear,* and Soft Matter Physics 92, no. 2: 1–15. https://doi.org/10 .1103/PhysRevE.92.022148
- Karimi-Fard, M., B. Gong, and L.J. Durlofsky. 2006. Generation of coarse-scale continuum flow models from detailed fracture characterizations. *Water Resources Research* 42, no. 10: 1–13. https://doi.org/10.1029/2006WR005015
- Keller, G.V., and F.C. Frischknecht. 1966. *Electrical Methods in Geophysical Prospecting*. Oxford, UK: Pergamon Press.
- Knox, J.C., A.D. Ebner, M.D. Levan, R.F. Coker, and J.A. Ritter. 2016. Limitations of breakthrough curve analysis in fixed-bed adsorption. *Industrial and Engineering Chemistry Research* 55, no. 16: 4734–4748. https://doi.org/10.1021/acs.iecr.6b00516
- Le Bars, M., and M.G. Worster. 2006. Interfacial conditions between a pure fluid and a porous medium: Implications for binary alloy solidification. *Journal of Fluid Mechanics* 550: 149–173. https://doi.org/10.1017/S0022112005007998
- Levy, M., and B. Berkowitz. 2003. Measurement and analysis of non-Fickian dispersion in heterogeneous porous media. *Journal of Contaminant Hydrology* 64, no. 3–4: 203–226. https://doi.org/10.1016/S0169-7722(02)00204-8
- Liu, Y., and P.K. Kitanidis. 2012. Applicability of the dual-domain model to nonaggregated porous media. *Ground Water* 50, no. 6: 927–934. https://doi.org/10.1111/j.1745-6584.2011.00909.x

- Liu, G., C. Zheng, G.R. Tick, J.J. Butler, and S.M. Gorelick. 2010. Relative importance of dispersion and rate-limited mass transfer in highly heterogeneous porous media: Analysis of a new tracer test at the macrodispersion experiment (MADE) site. Water Resources Research 46, no. 3: 1–8. https://doi.org/10.1029/2009WR008430
- Liu, G., C. Zheng, and S.M. Gorelick. 2007. Evaluation of the applicability of the dual-domain mass transfer model in porous media containing connected high-conductivity channels. *Water Resources Research* 43, no. 12: 1–12. https://doi.org/10.1029/2007WR005965
- MahmoodPoor Dehkordy, F.M., M.A. Briggs, F.D. Day-Lewis, and A.C. Bagtzoglou. 2018. Simulation of less-Mobile porosity dynamics in contrasting sediment water Interface porous media. *Hydrological Processes* 32, no. 13: 2030–2043. https://doi.org/10.1002/hyp.13134
- Major, E., D.A. Benson, J. Revielle, H. Ibrahim, A. Dean, R.M. Maxwell, E. Poeter, and M. Dogan. 2011. Comparison of Fickian and temporally nonlocal transport theories over many scales in an exhaustively sampled sandstone slab. Water Resources Research 47, no. 10: 1–14. https://doi.org/10.1029/2011WR010857
- Meigs, L.C., and R.L. Beauheim. 2001. Tracer tests in fractured dolomite, 1. Experimental design and observed tracer recoveries. *Water Resources Research* 37, no. 5: 1113–1128. https://doi.org/10.1029/2000WR900335
- Moradi, G., and B. Mehdinejadiani. 2018. Modelling solute transport in homogeneous and heterogeneous porous media using spatial fractional advection-dispersion equation. *Soil and Water Research* 13, no. 1: 18–28. https://doi.org/10.17221/245/2016-SWR
- Nagare, R.M., Y.J. Park, T. Butterfield, C. Belenky, and S. Scyrup. 2020. Analytical and numerical modeling of solute intrusion, recovery, and rebound in fractured bedrock. *Groundwater* 58, no. 1: 56–69. https://doi.org/10 .1111/gwat.12892
- Rao, P.S.C., R.E. Jessup, D.E. Rolston, J.M. Davidson, and D.P. Kilcrease. 1980. Experimental and mathematical description of nonadsorbed solute transfer by diffusion in spherical aggregates. Soil Science Society of America Journal 44, no. 4: 684–688. https://doi.org/10.2136/sssaj1980 .03615995004400040004x
- Scruggs, C.R., M. Briggs, F.D. Day-Lewis, D. Werkema, and J.W. Lane. 2019. The dual-domain porosity apparatus:

- Characterizing dual porosity at the sediment/water Interface. *Groundwater* 57, no. 4: 640–646. https://doi.org/10.1111/gwat.12846
- Singha, K., A. Pidlisecky, F.D. Day-Lewis, and M.N. Gooseff. 2008. Electrical characterization of non-Fickian transport in groundwater and hyporheic systems. Water Resources Research 46, no. 4: 1–14. https://doi.org/10.1029/2008WR007048
- Singha, K., F.D. Day-Lewis, and J.W. Lane Jr. 2007. Geoelectrical evidence of bicontinuum transport in groundwater. Geophysical Research Letters 34, no. 12: 1–5. https://doi.org/10.1029/2007GL030019
- Swanson, R.D., A. Binley, K. Keating, S. France, G. Osterman, F.D. Day-Lewis, and K. Singha. 2015. Anomalous solute transport in saturated porous media: Relating transport model parameters to electrical and nuclear magnetic resonance properties. Water Resources Research 51, no. 2: 1264–1283. https://doi.org/10.1093/acprof:oso/9780198506409.003.0024
- Swanson, R.D., K. Singha, F.D. Day-Lewis, A. Binley, K. Keating, and R. Haggerty. 2012. Direct geoelectrical evidence of mass transfer at the laboratory scale. Water Resources Research 48, no. 10: 1–10. https://doi.org/10.1029/2012WR012431
- Visentini, A.F., P. de Anna, D. Jougnot, T. Le Borgne, Y. Méheust, and N. Linde. 2023. Electrical signatures of diffusion-limited mixing: Insights from a milli-fluidic tracer experiment. *Transport in Porous Media* 146, no. 1–2: 435–461. https://doi.org/10.1007/s11242-021-01607-0
- Wheaton, D.D., and K. Singha. 2010. Investigating the impact of advective and diffusive controls in solute transport on geoelectrical data. *Journal of Applied Geophysics* 72, no. 1: 10–19. https://doi.org/10.1016/j.jappgeo.2010.06.006
- Zheng, C., M. Bianchi, and S.M. Gorelick. 2011. Lessons learned from 25 years of research at the MADE site. *Ground Water* 49, no. 5: 649–662. https://doi.org/10.1111/j.1745-6584.2010.00753.x
- Zheng, C., and G.D. Bennett. 2002. Applied Contaminant Transport Modeling, 2nd ed. New York: John Wiley and Sons. Inc.
- Zienkiewicz, O.C., R.L. Taylor, and P. Nithiarasu. 2013. The Finite Element Method for Fluid Dynamics, 7th ed. Amsterdam, the Netherlands: Elsevier Ltd.